# General hierarchical structure to solve transport phenomena with dissimilar time scales: Application in large-scale three-dimensional thermosolutal phase-field problems

Ang Zhang,[1,2,*] Jinglian Du,[1] Junye Yang,[1] Zhipeng Guo,[3,†] Qigui Wang,[4] Bin Jiang,[2] Fusheng Pan,[2] and Shoumei Xiong[1,5,‡]

[1]*School of Materials Science and Engineering, Tsinghua University, Beijing 100084, China*

[2]*National Engineering Research Center for Magnesium Alloys, Chongqing University, Chongqing 400044, China*

[3]*Institute for Aero Engine, Tsinghua University, Beijing 100084, China*

[4]*Materials Technology, GM Global Propulsion Systems, Pontiac, Michigan 48340-2920, USA*

[5]*Key Laboratory for Advanced Materials Processing Technology, Ministry of Education, Tsinghua University, Beijing 100084, China*

(Received 17 October 2019; revised 29 August 2020; accepted 23 September 2020; published 15 October 2020)

A general hierarchical structure is developed for phase-field lattice-Boltzmann simulations with dissimilar time scales. The number of the grid levels can be artificially selected in a reasonable range, which can enhance the time marching step by two to three orders of magnitude in comparison with explicit methods. Constructed on a massively parallel platform, the mesh distribution is dynamically adjusted according to a gradient criterion. The developed high performance computing scheme is applied to simulate the coupled thermosolutal dendrite evolution. Numerical tests indicate that the computing efficiency can be further improved by two to three orders of magnitude, which makes numerical simulation of fully coupled thermosolutal dendrite growth viable for alloys with Lewis number $\sim 10^4$. The domain size which equivalently consists of billions of uniform meshes is handled to simulate multidendrite evolution. Results show that the domain temperature becomes extremely uneven due to the release of latent heat, which causes a significant difference from isothermal solidification. A simple analytical model is proposed to predict the relation between growth velocity and Lewis number, and the growth morphologies of both equiaxed and directional multiple dendrites are discussed. The combination of the hierarchical mesh structure and the phase-field lattice-Boltzmann method provides an efficiency-driven approach to solve the coupled thermosolutal microstructure evolution.

DOI: 10.1103/PhysRevE.102.043313

## I. INTRODUCTION

Dendrite microstructure is one of the most common solidification patterns of alloys [1–3]. Starting from a stable nucleus, the solid-liquid (S-L) interface proceeds into the undercooled melt to maintain local thermodynamic equilibrium and evolves into a treelike microstructure named the *dendrite* [4].

The interaction between capillarity and thermosolutal transport during solidification determines eventual dendrite morphology, which significantly influences the mechanical properties of materials [5–7]. However, performing experiments to investigate the *microthermosolutal* transport is commonly infeasible due to a rather large Lewis number (i.e., $\mathrm{Le} = \alpha/D$, thermal diffusivity $\alpha$ divided by solutal diffusivity $D$). On the other hand, numerical modeling is a powerful tool to explore the microstructure evolution. The phase-field method (PFM) is becoming a standard computational approach to predict the mesoscale microstructure [8–11]. The most remarkable improvement of the PFM is that the interface width is assumed to be thin but finite, over which an order parameter, i.e., the phase field $\phi$, is introduced and it varies smoothly across the adjacent bulk phases. Besides, the explicit tracking of the interface is avoided, which greatly simplifies the complexity of the problem.

The simulation of dendrite evolution by the PFM has attracted considerable interest for decades, but most studies only focus on the pure solute diffusion by assuming that the heat diffuses infinitely fast. A so-called frozen temperature approximation [12–16] or isothermal solidification [17–21] is normally employed to decouple the solute field and the thermal field, which reduces the computing overhead but deviates from the practical solidification condition. Loginova *et al.* [22] found that the nonisothermal effect would become non-negligible for a larger cooling rate and fewer nuclei. Removing the isothermal assumption is essential to retrieve the true coupled thermosolutal dendrite evolution. However, to realize this, three major difficulties need to be addressed:

(1) For metallic alloys with $\mathrm{Le} \sim 10^4$, the time step during simulation must be sufficiently small, e.g., $10^{-10}$ s, to match the constraint limit for numerical stability, which significantly increases the computing overhead when a real time scale for the simulation is required.

(2) The mesh size must be small enough, e.g., $10^{-9}$–$10^{-8}$ m, to resolve the refined diffuse interface, which leads to a large number of grids if a real length scale is reproduced.

(3) To fully recover the underlying physics, three-dimensional (3D) simulations are mandatory to eliminate

*Corresponding author: angzhang@cqu.edu.cn

†Corresponding author: zhipeng_guo@mail.tsinghua.edu.cn

‡Corresponding author: smxiong@tsinghua.edu.cn

 ©2020 American Physical Society

the possible biased or inaccurate results in 2D simulations [21,23]. The 3D simulations are generally much more computationally intensive than the 2D cases.

A general and robust numerical scheme is needed to efficiently solve the three tough problems, especially the dissimilar time scales. Ramirez *et al.* [4] used a nonuniform grid to investigate the thermosolutal (Le $\sim$ 40) 2D dendrite growth. Rosam *et al.* [24,25] adopted an adaptive and implicit multigrid method to simulate the 2D thermosolutal (Le $\sim$ 200) dendrite solidification. Guo *et al.* [26] extended the multigrid algorithm with a highly parallelized computing scheme to simulate thermosolutal (Le $\sim 10^4$) multidendrite evolution. Nevertheless, the 3D phase-field simulation is still struggling due to its intensive computing overhead, especially when Le approaches $\sim 10^4$. Recently, the current authors [27] combined the parallel multigrid algorithm and mesh adaptivity, realizing 3D thermosolutal simulation (Le $\sim 10^4$). But this computing scheme is rather complicated and needs many iterations in each advancing step due to its implicit nature.

To improve the availability of the algorithm, in this work, a simpler numerical scheme is developed based on our latest work on 3D isothermal dendrite growth [28,29]. In detail, the PFM is used to simulate the dendrite evolution, and a kinetic-based approach, i.e., the lattice Boltzmann method (LBM), is employed to solve the evolution of the thermal field. It is worth stressing that the LBM shows good stability and high computing performance [30]. The LBM has been successfully combined with the PFM to simulate dendrite growth under convection [31,32] and is validated effective to simulate thermal evolution during solidification by Cartalade and co-workers [33,34].

Furthermore, a hierarchical structure with dynamically adjusted mesh distribution is developed to enable the large-scale phase-field lattice-Boltzmann (PFLB) simulations with dissimilar time scales. The restriction on the time marching step is eliminated by constructing a multilevel data structure and the number of grid levels can be artificially selected in a reasonable range. The computing efficiency is further improved by building the numerical scheme on a massively parallel platform, which enables the domain which equivalently comprises billions of meshes in a uniform-grid scheme to be processed. Both 2D and 3D single and multidendrites are discussed to illustrate the robustness of the numerical scheme. A simple analytical model is proposed to predict the relation between growth velocity and Lewis number. Influenced by the uneven temperature distribution, a significant difference is observed in the development of dendrite arms.

## II. MATHEMATICAL METHOD

### A. Phase-field model

A quantitative phase-field model coupled with thermosolutal diffusion proposed by Ramirez *et al.* [35] is employed to simulate dendrite evolution. The total free energy $F$ and corresponding governing equations for the phase field $\phi$, solute concentration $C$, and temperature $T$ are given by

$$F[\phi, C, T] = \int dV \left[\frac{\sigma}{2}|\nabla\phi|^2 + f_{\mathrm{AB}}(\phi, C, T)\right], \tag{1}$$

$$\frac{\partial\phi}{\partial t} = -K_\phi \frac{\delta F}{\delta\phi}, \tag{2}$$

$$\frac{\partial C}{\partial t} = \nabla\cdot\left(K_c\nabla\frac{\delta F}{\delta C} - \vec{j}_{\mathrm{at}}\right), \tag{3}$$

$$\frac{\partial T}{\partial t} = \alpha\nabla^2 T + \frac{L}{2c_p}\frac{\partial\phi}{\partial t} - \dot{q}, \tag{4}$$

where the phase field $\phi$ varies smoothly from 1 in solid to $-1$ in liquid, $\sigma$ is the gradient energy coefficient, and $f_{\mathrm{AB}}$ is the bulk free energy density of the dilute binary alloy including $A$ and $B$ components. $K_\phi$ and $K_c$ are constants, $L$ is the latent heat, and $c_p$ is the specific heat. $\dot{q} > 0$ is an imposed heat sink to simulate the heat flux out of the computational domain [26,36,37]. Without this additional term, the released latent heat will elevate the domain temperature and arrest solidification. $\vec{j}_{\mathrm{at}}$ is an antitrapping current introduced by Karma [38] to eliminate nonequilibrium effects at the diffuse interface,

$$\vec{j}_{\mathrm{at}} = -\frac{W}{\sqrt{2}}\frac{C/C_\infty}{1+k-(1-k)\phi}\frac{\partial\phi}{\partial t}\frac{\nabla\phi}{|\nabla\phi|}, \tag{5}$$

where $W$ is the interface thickness, $C_\infty$ is the initial solute concentration, and $k$ is the equilibrium partition coefficient.

According to the thin-interface analysis [35], the dimensionless phase-field equations can be expressed as follows:

$$\begin{aligned} A(\hat{n})^2\left[\frac{1}{\mathrm{Le}} + k[1+(1-k)U]\right]\frac{\partial\phi}{\partial\tilde{t}} &= \frac{1}{2}\nabla\cdot\left[\frac{\partial[A(\hat{n})^2|\nabla\phi|^2]}{\partial\nabla\phi}\right] \\ &\quad + \phi - \phi^3 - \lambda(1-\phi^2)^2(\theta + kU), \end{aligned} \tag{6}$$

$$\begin{aligned} \frac{1+k-(1-k)\phi}{2}\frac{\partial U}{\partial\tilde{t}} &= \nabla\cdot\left[\tilde{D}\frac{1-\phi}{2}\nabla U - \vec{j}_{\mathrm{at}}\right] \\ &\quad + \frac{1+(1-k)U}{2}\frac{\partial\phi}{\partial\tilde{t}}, \end{aligned} \tag{7}$$

$$\frac{\partial\theta}{\partial\tilde{t}} = \tilde{\alpha}\nabla^2\theta + \frac{1}{2}\frac{L/c_p}{\Delta T_0}\frac{\partial\phi}{\partial\tilde{t}} - \tilde{q}, \tag{8}$$

where $A(\hat{n})$ is the anisotropy function, which reflects the anisotropy of the interfacial energy [35,39], and $\hat{n} = -\nabla\phi/|\nabla\phi|$ is the unit vector normal to the interface. $\tilde{\alpha} = \mathrm{Le}\lambda a_2$, $\tilde{D} = \lambda a_2$, and $\tilde{\dot{q}} = \dot{q}\tau_0/\Delta T_0$ are the dimensionless thermal diffusivity, dimensionless solutal diffusivity, and dimensionless heat sink respectively, where the time, length, and temperature are scaled by $\tau_0 = d_0^2 a_2\lambda^3/(Da_1^2)$, $W_0 = \lambda d_0/a_1$, and the equilibrium freezing temperature range $\Delta T_0 = |m|C_\infty(1-k)/k$. $d_0 = \Gamma/\Delta T_0$ is the chemical capillary length, $\Gamma$ is the Gibbs-Thomson coefficient, $m$ is the liquidus slope, $a_1 = 0.8839$, $a_2 = 0.6267$, and $\lambda$ is a coupling constant defined as

$$\lambda = \frac{15RT_M(1-k)}{16\upsilon_0 H|m|}\Delta T_0, \tag{9}$$

where $R$ is the gas constant, $T_M$ is the melting point of the pure solvent, $\upsilon_0$ is the molar volume, and $H$ is the energy barrier of the double well potential. $U$ and $\theta$ are the dimensionless solute concentration and dimensionless temperature, and they

are defined as follows:

$$U = \frac{\frac{2C/C_\infty}{1+k-(1-k)\phi} - 1}{1-k}, \tag{10a}$$

$$\theta = \frac{T - T_M - mC_\infty}{\Delta T_0}. \tag{10b}$$

$\theta < 0$, and the dimensionless undercooling defined by $\Delta = -\theta$ is specified in the following simulations.

For the crystal with cubic symmetry, the anisotropy function $A(\hat{n})$ in the 3D case can be expressed as follows [39]:

$$A(\hat{n}) = 1 + \varepsilon_1(Q - 3/5) + \varepsilon_2(3Q + 66S - 17/7), \tag{11a}$$

$$Q = \frac{\phi_{\tilde{x}}^4 + \phi_{\tilde{y}}^4 + \phi_{\tilde{z}}^4}{|\nabla\phi|^4}, \tag{11b}$$

$$S = \frac{\phi_{\tilde{x}}^2\phi_{\tilde{y}}^2\phi_{\tilde{z}}^2}{|\nabla\phi|^6}, \tag{11c}$$

where $\phi_{\tilde{i}} = \partial\phi/\partial\tilde{i}$ ($i = x$, $y$, or $z$.), $\varepsilon_1$ and $\varepsilon_2$ are the weight coefficients favoring $\langle 100\rangle$ and $\langle 110\rangle$ dendrite growth directions, respectively. For the 2D case, the anisotropy function is expressed as $A(\hat{n}) = 1 + \varepsilon\cos 4(\psi - \psi_0)$ [35], where $\varepsilon$ denotes the anisotropy strength, $\psi = \arctan(\phi_{\tilde{y}}/\phi_{\tilde{x}})$ is the angle between the primary arm and the $x^+$ axis, and $\psi_0$ is the predefined growth orientation.

When simulating multidendrite growth with random growth orientations, a much simpler method is employed to avoid introducing extra equations describing the orientation field [37]. The solid nuclei with predefined orientations are initialized in the computational domain. As the solidification proceeds, a small quantity of liquid is transformed into the solid, and the solid increment is assumed to have the same orientation as that of the original, which is equivalent to that the dendrite grows by imposing its orientation on its nearest liquid. This method is physically closer to the practical solidification condition and has been validated in our previous work including the 2D case [26] and 3D isothermal case [28].

### B. Lattice Boltzmann method

As a mesoscopic kinetic method, the LBM assumes that the *macro* fluid is comprised of a collection of pseudoparticles represented by a distribution function [40]. The transport phenomena are revealed by the local streaming and collision of those particles [40]. For the heat transport in this work, a widely used approximation named the lattice Bhatnagar-Gross-Krook (LBGK) model [41] is employed to solve the thermal evolution [i.e., Eq. (8)], and the corresponding governing equation is expressed as

$$f_i(\vec{r} + \delta\vec{r}, t_{\rm LBM} + \delta t) = f_i(\vec{r}, t_{\rm LBM}) - \frac{1}{\tau_{\rm LBM}}[f_i(\vec{r}, t_{\rm LBM}) - f_i^{\rm eq}(\vec{r}, t_{\rm LBM})] + F_i(\vec{r}, t_{\rm LBM})\delta t, \tag{12}$$

where $f_i(\vec{r}, t_{\rm LBM})$ is the particle distribution function along the $i$th direction, which represents the number of the particles at the position $\vec{r}$ and time $t_{\rm LBM}$. $\tau_{\rm LBM}$ is the relaxation time related to the thermal diffusivity $\alpha_{\rm LBM}$ in the LBM, i.e., $\alpha_{\rm LBM} = c^2\delta t(2\tau_{\rm LBM} - 1)/6$, where $c = \delta x/\delta t$ is the lattice speed, $\delta x$ is the lattice spacing, and $\delta t$ is the time step in the LBM, both of which are formally rescaled to 1. $f_i^{\rm eq}(\vec{r}, t_{\rm LBM}) = w_i\theta$ is the equilibrium distribution function accounting for the diffusion effect [42], where $w_i$ is the weight coefficient determined by the discrete velocity model, i.e., $w_0 = 4/9$, $w_{1-4} = 1/9$, and $w_{5-8} = 1/36$ for the 2D nine-velocity model named D2Q9, and $w_0 = 1/3$, $w_{1-6} = 1/18$, and $w_{7-18} = 1/36$ for the 3D 19-velocity model named D3Q19. The macroscopic temperature and the discrete force reflecting the source term in Eq. (8) are expressed as follows [43]:

$$\theta = \sum_i f_i + \frac{\delta t}{2}\left(\frac{1}{2}\frac{L/c_p}{\Delta T_0}\frac{\partial\phi}{\partial t_{\rm LBM}} - \dot{q}_{\rm LBM}\right), \tag{13a}$$

$$F_i(\vec{r}, t_{\rm LBM}) = \left(1 - \frac{1}{2\tau_{\rm LBM}}\right)w_i\left(\frac{1}{2}\frac{L/c_p}{\Delta T_0}\frac{\partial\phi}{\partial t_{\rm LBM}} - \dot{q}_{\rm LBM}\right), \tag{13b}$$

where $\dot{q}_{\rm LBM}$ is the imposed heat sink in the LBM, and the coefficient $(1–1/2\tau_{\rm LBM})$ in Eq. (13b), together with the second term on the right side of Eq. (13a), is to eliminate the unwanted term during the Chapman-Enskog analysis [30,43].

## III. NUMERICAL APPROACH

### A. Discretization of equations

The discretization of the phase-field equations is performed on a Cartesian uniform grid. Taking Eq. (6) for instance, the central difference scheme is employed for the gradient term $\nabla$, and a net flux control volume approach is applied for the divergence operator $\nabla\cdot$. In detail, the variable is fixed at the cell center and its divergence is determined by summing the fluxes at cell walls, i.e., $\nabla\cdot J = \sum_i (J_{i^+} - J_{i^-})/d\tilde{x}$, where $i = x, y, z$, $d\tilde{x}$ is the space step, and $J_{i^+}$ and $J_{i^-}$ are the fluxes at the opposite walls.

The flux along the $x^+$ direction can be deduced from the first term on the right of Eq. (6), i.e.,

$$J_{x^+} = A(x^+)^2\phi_{\tilde{x}} + |\nabla\phi|^2 A(x^+)\partial[A(x^+)]/\partial\phi_{\tilde{x}}, \tag{14a}$$

where $J = \partial[A(\hat{n})^2|\nabla\phi|^2]/\partial(\nabla\phi)$, and $A(x^+)$ is the anisotropy function at the $x^+$ wall.

Similarly, the divergence operator in Eq. (7) can be written as $JS = 0.5\tilde{D}(1-\phi)\nabla U - \vec{j}_{\rm at}$, and thus the discretization form is expressed as follows in terms of the $x^+$ direction:

$$JS_{x^+} = \tilde{D}\frac{1-\phi}{2}\frac{\partial U}{\partial\tilde{x}} + \frac{\sqrt{2}}{4}[1 + U(1-k)]\frac{\partial\phi}{\partial\tilde{t}}\frac{\phi_{\tilde{x}}}{|\nabla\phi|}. \tag{14b}$$

A first-order forward Euler stepping scheme is adopted to update the phase field and solute field, taking the phase-field variable for instance, i.e.,

$$\left.\frac{\partial\phi}{\partial\tilde{t}}\right|^n = \frac{\phi^n - \phi^{n-1}}{d\tilde{t}}, \tag{15}$$

where $d\tilde{t}$ is the time step during simulation, and the superscripts $n$ and $n-1$ denote the time.

### B. Hierarchical mesh structure

A hierarchical mesh architecture with block-structure adaptive mesh refinement (AMR) is constructed to solve the

PFLB equations. This multilevel structure has been successfully used to simulate the isothermal dendrite [28,44,45] and eutectic growth [46–49]. The key idea of this scheme is to tag the cells that need to be refined and then to separate them into clusters.

The refinement process is proceeded by first tagging the potential grids according to a predefined gradient criterion,

$$|\nabla\phi| + E_U|\nabla U| + E_\theta|\nabla\theta| \geqslant \xi, \tag{16}$$

where $E_U$ and $E_\theta$ are the weight coefficients for solute concentration and temperature respectively, and $\xi$ is a threshold value determined via numerical tests.

The S-L interface is the position where the gradient reaches the local extremes and hence the refinement is required. After a certain number of grids are tagged, a cluster algorithm developed by Berger and Rigoutsos [50] is adopted to separate the tagged grids into clusters or patch boxes which are actually rectangles in two dimensions but boxes with interior boundaries in three dimensions. The patch box consists of a collection of meshes with the same size. Starting from the bottom (i.e., the coarsest) grid level, the tagged grids are refined by subdividing the mesh with a predefined refining ratio (i.e., 2), and the refinement process continues until the required finest grid level is reached. It is noted that the layout of the patch boxes on each grid level must be correctly nested, i.e., the finer grids must be located inside the coarser ones.

After constructing a hierarchical structure with different sets of patch boxes on each grid level, the computing data including the phase field, solute concentration, and temperature needs to be communicated among different patch boxes at each time step. For that, a layer of ghost cells is added at the external boundaries of each patch box to collect the data from its closest neighbors. The values at the coarse level are updated by performing the restriction operation, i.e., updating values through the weighted average from the fine ones covering it, while those at the fine level are updated by interpolation operation using the data in the underlying coarse grid.

To maintain the thermal diffusivity constant in different levels, the relaxation time $\tau_{\mathrm{LBM}}$ in the multilevel structure needs to vary with the grid size [51], i.e.,

$$\tau_{\mathrm{LBMf}} = 2(\tau_{\mathrm{LBMc}} - 1/2) + 1/2, \tag{17}$$

where $\tau_{\mathrm{LBMf}}$ and $\tau_{\mathrm{LBMc}}$ are the relaxation time at the fine and coarse grid levels respectively. In addition, to ensure the continuity of the physical quantities over the coarse-fine interface, special attention is paid to the distribution function, which is rewritten as the sum of the equilibrium and nonequilibrium parts [51],

$$f_i^f(\vec{r}, t_{\mathrm{LBM}}) = \alpha\bar{f}_i^c(\vec{r}, t_{\mathrm{LBM}}) + (1-\alpha)f_i^{\mathrm{eq},f}(\vec{r}, t_{\mathrm{LBM}}), \tag{18a}$$

$$f_i^c(\vec{r}, t_{\mathrm{LBM}}) = 1/\alpha\hat{f}_i^f(\vec{r}, t_{\mathrm{LBM}}) + (1-1/\alpha)f_i^{\mathrm{eq},c}(\vec{r}, t_{\mathrm{LBM}}), \tag{18b}$$

where $\alpha = 0.5\,\tau_{\mathrm{LBMf}}/\tau_{\mathrm{LBMc}}$ is a weight coefficient, and the superscripts $f$ and $c$ denote the fine and coarse grid level respectively. $\bar{f}_i$ denotes the spatially and temporally interpolated distribution function of the coarse level, and $\hat{f}_i$ denotes the restricted values of the fine level.

To maintain the lattice velocity at one at any grid level, a multistep advancing approach is employed in the multilevel structure. In detail, after one "streaming and collision" step on the coarsest grid level, $2^{ld}$ "streaming and collision" steps need to be proceeded on the subsequent fine grid level [52], where $ld$ is the level difference between the coarsest and chosen fine grid level.

It is noted that there are three dimensions adopted in the PFLB method, i.e., actual → PFM → LBM. In particular, $t \to \tilde{t} \to t_{\mathrm{LBM}}$ and $x \to \tilde{x} \to x_{\mathrm{LBM}}$ for time and length respectively, which satisfy $\tilde{t} = t/\tau_0$, $t_{\mathrm{LBM}} = \tilde{t}/d\tilde{t}$ for time, and $\tilde{x} = x/W_0$, $x_{\mathrm{LBM}} = \tilde{x}/d\tilde{x}_{\max}$ for length. $d\tilde{x}_{\max}$ is the grid size at the coarsest grid level, which acts as the length unit for scaling length in the LBM because the quantities in the multilevel structure must be advanced from the coarsest to the finest grid level, i.e., from "bottom to top" [53]. $d\tilde{t}$ is restricted by the stability of the explicit algorithm, i.e.,

$$d\tilde{t} = \frac{r d\tilde{x}_{\min}^2}{2N_d\tilde{D}}, \tag{19}$$

where $r$ is an introduced stability coefficient, $d\tilde{x}_{\min}$ is the grid size at the finest grid level, $N_d$ is the dimension of the domain (i.e., 2 and 3 for the 2D and 3D cases respectively).

An outstanding advantage of the multilevel PFLB method over the direct solution to the thermal evolution equation (8) is that the constraint on the time step becomes much less restricted. According to Eq. (19), the time step needs to be inversely proportional to the diffusivity for explicit methods. Because Le is $\sim 10^4$ for metallic alloys, if Eq. (8) is explicitly discretized, the time step will be reduced by four orders of magnitude compared with that determined by Eq. (19), which requires a very long simulation time to approach the real case. On the contrary, if the LBM is employed to determine the thermal evolution, the time step can still be determined by Eq. (19) after choosing a proper stability coefficient $r$ (see the detailed derivation in the Appendix), i.e.,

$$r = (\tau_{\mathrm{LBM}} - 0.5)\frac{N_d 2^{2n_l-1}}{3\mathrm{Le}}, \tag{20}$$

where $n_l$ is the number of the grid levels in the hierarchical structure with a refining spacing ratio of 2 (i.e., the mesh size of the coarse grid level is two times larger than that of the neighboring fine level).

Accordingly, if $N_d = 3$ and $\mathrm{Le} = 1 \times 10^4$, we can choose $n_l = 5$, $\tau_{\mathrm{LBM}} = 1.08$, and thus $r = 0.03$, which is magnified by 300 times in comparison with the constraint limit in the explicit methods. In addition, the number of the grid levels can be artificially selected in a reasonable range. $n_l$ is related to $\tau_{\mathrm{LBM}}$, and $\tau_{\mathrm{LBM}}$ is advised to approach 1 [30]. A larger $\tau_{\mathrm{LBM}}$ can cause larger numerical error, while a lower one (i.e., close to 0.5) might lead to numerical instability. $n_l$ is not limited to a specific value, and there are infinite pairs of $(r, n_l)$. Table I lists some reference values based on Eq. (20) for different Le in three dimensions, in which "Magnification" denotes the magnification of the time step compared with that in the explicit finite difference method. The number of the grid levels can be up to 50 theoretically if more sophisticated method is combined to ensure numerical accuracy and stability [52].

Furthermore, the simplicity of explicit formulations in the LBM offers enhanced efficiency without any major change in

TABLE I. Reference values based on Eq. (20) for different Le in three dimensions.

| Case | Le | $n_l$ | $\tau_{\mathrm{LBM}}$ | $r$ | Magnification |
|---|---|---|---|---|---|
| 1 | $1 \times 10^3$ | 4 | 1.28 | 0.1 | ∼100 |
| 2 | $1 \times 10^4$ | 5 | 1.08 | 0.03 | ∼300 |
| 3 | $1 \times 10^5$ | 6 | 0.99 | 0.01 | ∼1000 |
| 4 | $1 \times 10^6$ | 7 | 1.11 | 0.005 | ∼5000 |
| 5 | $1 \times 10^7$ | 8 | 1.11 | 0.002 | ∼20000 |

the algorithmic structure. The solution of the expensive matrix problem during implicit time marching is avoided, which enforces the conservation laws by improving the round-off precision [54].

### C. Parallel computing scheme

After the adaptive mesh is generated, the overall mesh structure, together with the computing data, is broadcast to all processes, based on which the computing work is constructed, partitioned, and dispatched. Consequently, each process has its own but different data according to the local array of patch boxes, achieving the so-called single program with multiple data (SPMD).

The data partitioning, dispatching, and communication are controlled by a message passing library named the Message Passing Interface [55], which handles all data on a distributed memory level. A method based on the space filling curve [56] is adopted to avoid load imbalance of the computing data.

### D. Summary of the numerical scheme

The overall numerical scheme is organized as follows:

(1) Initialize the computational domain.

(2) Construct a hierarchical data structure by tagging and clustering operations based on Eq. (16).

(3) Broadcast the grid architecture to all processes to realize the parallelization of the computing data.

(4) Computation on each process:

```
for step = 1 : n_t
  for grid level = 1 : n_l
    for i_p = 1 : n_p
      solve Eqs. (6) and (7);
      solve Eqs. (12), (13a), and (13b);
    end
  end
  data communication among patch boxes and grid levels;
  at specified step, reconstruct the grid architecture according to Eq. (16);
end,
```

where $n_t$, $n_l$, and $n_p$ are the number of the total steps, the number of the grid levels and the number of the patch boxes, respectively, and $i_p$ is the index of the patch box on the certain grid level.

TABLE II. Scaling parameters used for the simulations.

| Parameter | Value |
|---|---|
| $\tau_0$ (time scale in the PFM, s) | $1.155 \times 10^{-4}$ |
| $dt$ (time step, s) | $1.638 \times 10^{-8}$ |
| $d_0$ (chemical capillary length, m) | $4 \times 10^{-9}$ |
| $W_0$ (interface width, m) | $1.358 \times 10^{-7}$ |
| $dx_{\mathrm{min}}$ (minimum spacing step, m) | $1.086 \times 10^{-7}$ |
| $\Delta T_0$ (freezing range, K) | 60 |

## IV. NUMERICAL TEST

The Al-4 wt % Cu alloy, physical parameters of which can be found elsewhere [26,57], is simulated in this work. The PFM is established and employed as a dimensionless form, and the scaling parameters used for the simulations are listed in Table II. The computational domain is a square (cube) filled with the undercooled melt for 2D (3D) cases. For the equiaxed dendrite, a zero-Neumann boundary condition is applied at all sides for all variables including the phase field, solute concentration, and temperature. The initial shape of the predefined solid seeds is circular (spherical) with the initial radius being 6.4 $W_0$ for 2D (3D) cases. The physical properties of materials are assumed constant, and the solute diffusion in the solid is neglected.

### A. Accuracy test

The phase-field model has been exhaustedly studied by direct comparisons with experiments in our previous work [3,28,29]. To test the accuracy of the temperature field calculated by the LBM, the diffusion equation coupled with the heat sink, i.e., Eq. (4), is solved on a domain $[-1,1] \times [-1,1]$ by both the finite difference method (FDM) and the LBM. The dimensionless physical quantities are set as $\alpha = 1, L = 0$, and $\dot{q} = 0.2$. All boundary conditions are zero Neumann. The temperature distribution is initialized as $T(t = 0) = 1 + \exp(-100 r_d^2)$, where $r_d$ is the distance from the point (0.25, 0.25) in the 2D case and (0.25, 0.25, 0.25) in the 3D case, respectively.

Taking the 3D case for instance, based on the explicit FDM, Eq. (4) is discretized as

$$T_{i,j,k}^{n+1} = \mathrm{Fo}\big(T_{i+1,j,k}^{n} + T_{i-1,j,k}^{n} + T_{i,j+1,k}^{n} + T_{i,j-1,k}^{n} + T_{i,j,k+1}^{n} + T_{i,j,k-1}^{n}\big) + (1 - 6Fo) T_{i,j,k}^{n} - \dot{q} dt, \quad (21)$$

where the superscripts $n$ and $n+1$ denote the time, the subscripts $i$, $j$, and $k$ denote the position, and the Fourier number $Fo$ is $dt/dx^2$. The scheme can keep stable by using a fixed time step $dt = r dx^2/(2N_d)$, where the stability coefficient $r$ should satisfy $0 < r \leqslant 1$.

The *macro* thermal evolution equation is transformed into the lattice-Boltzmann equation by the Chapman-Enskog analysis [42,58], and corresponding parameters in the LBM are $r = 0.9$, $\tau_{\mathrm{LBM}} = 0.5 + 3r/(2N_d)$, and $F_i(\vec{r}, t_{\mathrm{LBM}}) = -(1 - 1/2\tau_{\mathrm{LBM}}) w_i \dot{q} dt$. The D2Q9 and D3Q19 discrete velocity models are employed for the 2D and 3D cases, respectively. Figure 1 shows the predicted temperature versus the distance along the horizontal centerline (i.e., $y = Y/2$ for the 2D case and $y = Y/2$, $z = Z/2$ for the 3D case, where $X$,

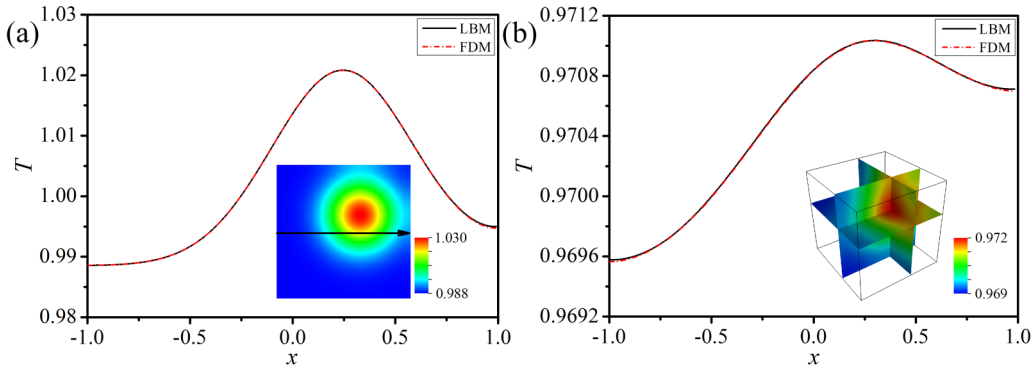


FIG. 1. Temperature distribution along the horizontal centerline for (a) 2D and (b) 3D cases, respectively. Both $T$ and $x$ are dimensionless.

$Y$, $Z$ are the domain length) at the 4000th steps with inset temperature field cloud maps. The temperature-distance curves overlap, indicating that the calculated results by the LBM agree quite well with those by the FDM. Table III shows the maximum and minimum of the particle distribution functions $f_i$. Despite the difference in the numerical values of $f_i$, the cloud maps are basically similar to the insets in Fig. 1 except for a small amount of offset in position.

### B. Efficiency test

The computing efficiency is tested by changing the number of the parallel processes $n_p$ and the number of the grid levels $n_l$. The seed is initialized at the domain center, and the dimensionless minimum mesh size $d\tilde{x}_{\min}$ is 0.8. The following parameters are adopted until stated otherwise: For the 2D case, $\Delta = 0.2$. $\lambda = 10$, $\varepsilon = 0.02$, $r = 0.01$, while for the 3D case, $\Delta = 0.12$, $\lambda = 30$, $\varepsilon_1 = 0.1$, $\varepsilon_2 = 0$, $r = 0.05$. The stability coefficient $r$ is significantly larger than that used in the explicit difference method, i.e., the time step is enhanced by 100 and 500 times for the 2D and 3D cases respectively.

The domain size is $1024 \times 1024$ and $512 \times 512 \times 512$ in 2D and 3D cases respectively, i.e., $819.2 \times 819.2$ units of ${W_0}^2$ and $409.6 \times 409.6 \times 409.6$ units of ${W_0}^3$ if a uniform grid $dx = 0.8$ units of $W_0$ is employed. The total computing steps are 500 000 and 50 000 steps for the 2D and 3D cases, and the corresponding memory consumption is 1.8 and 24 GB respectively, which is accessible for today's computers (e.g., a single workstation with 64 GB memory). Figure 2 shows the total elapsed time varying with $n_p$ and $n_l$. It is noted that when $n_p = 1$ and $n_l = 1$, the current algorithm is restored to the normally applied algorithm without acceleration. In this case, it takes about 50 758 s in the 2D case. When $n_p$ reaches 32, the elapsed time is shortened to 1993 s, i.e., gaining 25 times speedup, which is lower than the theoretical prediction (i.e., 32) due to the inevitable data communication among processes. Besides, because the amount of computing data is not enough to be dispatched to each process, no further computing speedup is achieved when $n_p$ exceeds 24 for the 2D case with three grid levels and 144 for the 3D case with five grid levels.

TABLE III. Maximum (Max.) and minimum (Min.) of the distribution function $f_i$ in the LBM.

| Case | $f_i$ | Max. | Min. |
|---|---|---|---|
| 2D | $f_0$ | 0.4578 | 0.4393 |
| | $f_1$–$f_4$ | 0.1145 | 0.1098 |
| | $f_5$–$f_8$ | 0.028 61 | 0.027 46 |
| 3D | $f_0$ | 0.3238 | 0.3231 |
| | $f_1$–$f_6$ | 0.053 97 | 0.053 85 |
| | $f_7$–$f_{18}$ | 0.026 99 | 0.026 92 |

Remarkable improvement in efficiency is also observed by applying the mesh adaptivity. Taking the 3D case in Fig. 2(b) for instance, when $n_p = 48$, the elapsed time decreases from 91 906 s at $n_l = 1$ to 9511 s at $n_l = 5$, i.e., speeding up $\sim$10 times in efficiency. The construction of the multilevel structure decreases the total computing data and thus improves the computing efficiency. Further increasing $n_p$ also shortens the computing time. With a combination of $n_l = 5$ and $n_p = 144$, the total computing time is shortened to 4303 s. Similar to the efficiency improvement by only increasing $n_p$, no more significant acceleration is observed when $n_l$ reaches a certain value, e.g., $n_l$ increases from 3 to 4 when $n_p = 8$ for the 2D case, because building the complicated hierarchical architecture will consume much of the total elapsed time. Nevertheless, the combination of the parallel computing and adaptive hierarchical structure greatly reduces the computing overhead and shortens the simulation time by two to three orders of magnitude in comparison with the normally applied algorithm without acceleration.

Furthermore, as designated by "$L_1$" and "$L_2$" in Fig. 2, the logarithm of the total elapsed time $t_{\text{simu}}$ decreases nearly lineally with $\log_2 n_p$, which can be described as

$$\log_{10} t_{\text{simu}} = k \log_2 n_p + \log_{10} t_{\text{simu}}^{n_p=1}, \tag{22}$$

where $k$ is the slope, and $t_{\text{simu}}^{n_p=1}$ is the elapsed time for the case where $n_p = 1$. The slopes of the lines "$L_1$" and "$L_2$" are $-0.2848$, $-0.2512$ for the 2D cases, and $-0.2392$, $-0.2048$ for the 3D cases, respectively. To maximize the utilization of the computing resource, the number of the parallel processes and the number of the grid levels should be chosen reasonably before simulation.

### C. Influence of heat sink

When the thermal evolution is considered into the dendrite evolution, an imposed heat sink $\dot{q}_{\text{LBM}}$ is introduced to avoid

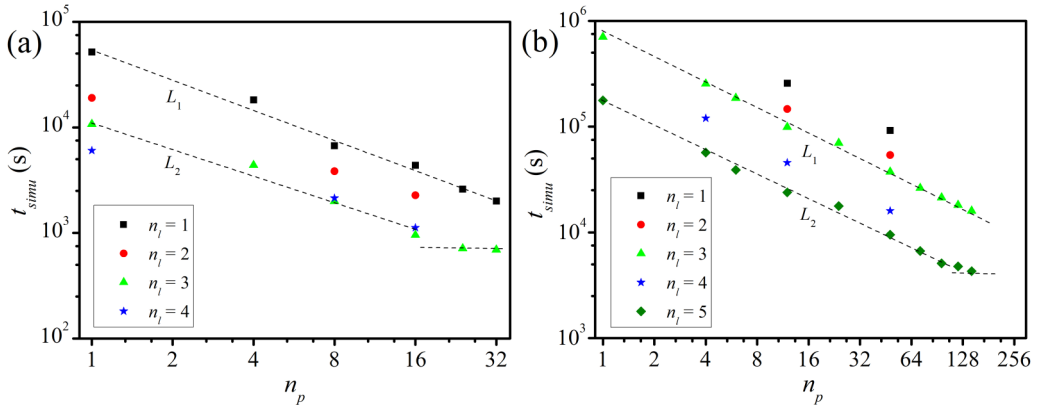


FIG. 2. Efficiency test for (a) 2D and (b) 3D cases by using the developed numerical algorithm to solve the thermosolutal PFLB equations. $n_p$ is the number of the parallel processes, and $n_l$ is the number of the grid levels employed during simulation.

the continuous temperature rise induced by the release of latent heat. $\dot{q}_{\mathrm{LBM}}$ influences the dendrite morphology by uniformly changing the total undercooling. To investigate such effect, the dendrite morphology under different heat sink is compared.

Figure 3 shows the average growth velocity of the 2D dendrite tip versus the magnitude of the heat sink. The insets show the thermal distribution (on the left side) and the dendrite contour with the patch-box architecture (on the right side). The closer to the S-L interface, the finer the mesh size, and the higher the temperature due to the release of latent heat. Because of the large difference of the growth velocity under different thermal conditions, the average growth velocity is used instead. The average growth velocity is calculated by the distance divided by the required elapsed time when the dendrite reaches the same domain position (see the insets). For a relatively small heat sink, e.g., $\dot{q}_{\mathrm{LBM}} = 1 \times 10^{-7}$, the dendrite grows slowly because a large amount of heat is accumulated near the S-L interface, lowering the local undercooling. Similar to that induced by increasing local solute concentration, the accumulated heat widens the primary arms [3]. As the heat sink increases, the temperature is efficiently reduced, which increases the undercooling and accelerates the dendrite growth. When the heat sink is large enough, e.g., $\dot{q}_{\mathrm{LBM}} = 5 \times 10^{-6}$, the dendrite morphology becomes square due to increasingly developed side arms, i.e., the crystal anisotropy is significantly weakened.

Figure 4 shows the simulated 3D dendrite morphology with $\dot{q}_{\mathrm{LBM}}$ being $5 \times 10^{-6}$, $1 \times 10^{-5}$, $5 \times 10^{-5}$, and $1 \times 10^{-4}$ respectively. Each column corresponds to the same heat sink, and the first and second rows show the dendrite morphologies viewed from [100] and [111] directions respectively. A smaller heat sink corresponds to more accumulated heat, which decreases the driving force for solidification and causes less developed side branches. When the heat sink is relatively large, e.g., $\dot{q}_{\mathrm{LBM}} \geqslant 5 \times 10^{-6}$, the side arms become highly developed.

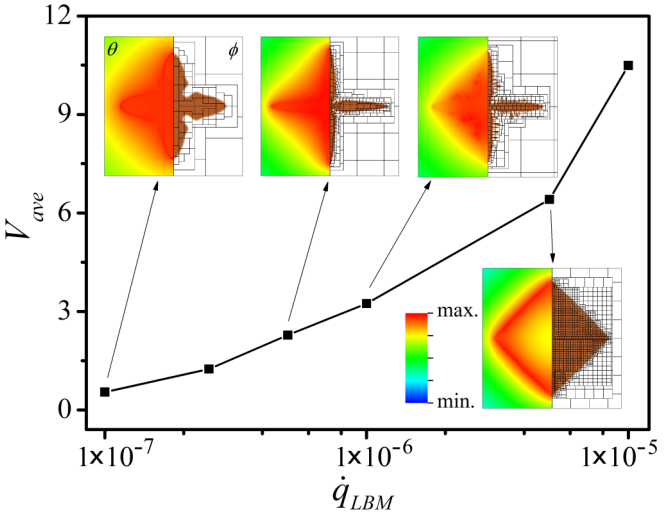


FIG. 3. Dimensionless average growth velocity $V_{\mathrm{ave}}$ of the 2D dendrite tip versus heat sink $\dot{q}_{\mathrm{LBM}}$. The insets show the thermal distribution (on the left side) and the dendrite contour with the patch-box architecture (on the right side).

## V. RESULTS AND DISCUSSION

### A. Single dendrite growth

Figure 5 shows the simulation results of the single dendrite including the phase field, solute field, temperature field, and typical hierarchical structure of the patch boxes. In Fig. 5(a), the domain size is 4096 × 4096 (i.e., 3276.8 × 3276.8 units of $W_0{}^2$ when $dx_{\mathrm{min}} = 0.8$ units of $W_0$), and $\dot{q}_{\mathrm{LBM}} = 5 \times 10^{-7}$.

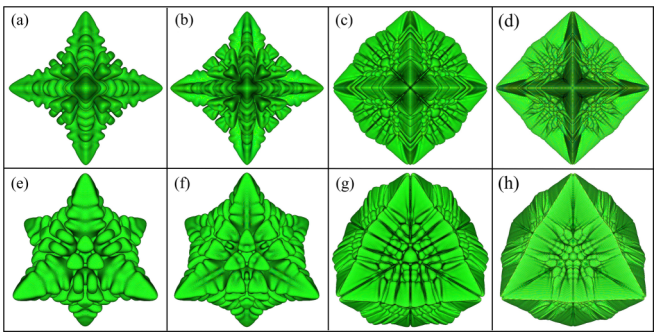


FIG. 4. 3D dendrite morphology with $\dot{q}_{\mathrm{LBM}}$ being $5 \times 10^{-6}$, $1 \times 10^{-5}$, $5 \times 10^{-5}$, and $1 \times 10^{-4}$ from (a) to (d) [or from (e) to (h)] respectively. The first and second rows show the dendrite morphologies viewed from the [100] and [111] directions respectively.

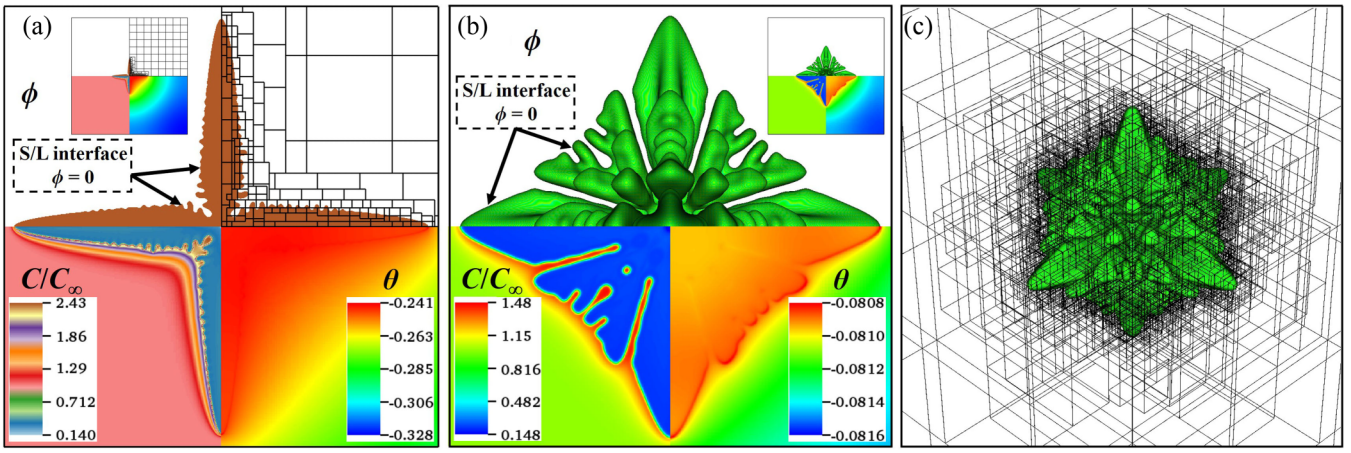


FIG. 5. Simulated single dendrite morphology including the phase field, solute field, temperature field, and hierarchical structure of the patch boxes during the AMR for (a) 2D and (b) 3D case. (c) Hierarchical grid structure according to the AMR for the 3D single dendrite.

The dendrite is magnified from the original size which is inset in the upper-left quadrant to present the detailed structure. A general fourfold symmetric morphology exhibits, and some side arms start to stretch out along the direction perpendicular to the primary arms. Influenced by the curvature effect, the rejected solute becomes enriched between those protruding side branches, causing local solute accumulation, which agrees well with those reported by Ramirez *et al.* [4,35]. In the bottom-left quadrant, an intricate microsegregation pattern is predicted in the solid region. Besides, as expected from a large Le, the thickness of the thermal boundary layer is noticeably larger than that of the solutal boundary layer. Because of the release of latent heat, the recalescence behavior occurs, and the temperature in solid is higher than that in liquid. The temperature gradually decreases with the distance away from the interface. In the upper-right quadrant, a hierarchical grid structure is presented, in which the S-L interface is properly characterized by the layout of the patch boxes at the top (i.e., the finest) grid level.

Figure 5(b) shows the 3D dendrite morphology including the phase field, solute field, and temperature field. The domain size is $1024 \times 1024 \times 1024$ (i.e., $819.2 \times 819.2 \times 819.2$ units of ${W_0}^3$ when $dx_{\min} = 0.8$ units of $W_0$), which is equivalent to over one billion meshes if a uniform mesh structure is employed. $\dot{q}_{\mathrm{LBM}} = 0$. The highest temperature appears near the S-L interface, and the width of the thermal boundary layer is larger than that of the solutal boundary layer. Six primary arms grow out from the seed center and gradually evolve into a paraboloid shape. Figure 5(c) shows the hierarchical grid structure according to the AMR. It is worth stressing that the boxes are not grid cells but rather patch boxes as discussed in Sec. III B. The layout of the patch boxes clearly illustrates that the AMR can perfectly characterize the S-L interface, which reduces the computing overhead and makes the 3D simulations in a larger computational domain feasible. In comparison with the pyramidal dendrite envelope reported by Bragard *et al.* [59], a fully evolving dendrite with more detailed features is reproduced, especially the evolution of the secondary arms.

Figure 6 shows the dimensionless temperature versus the distance along the horizontal centerline of the 2D domain corresponding to Fig. 5(a) at the 300 000th, 600 000th, and 1 000 000th steps respectively. The temperature obtains the maximum at the dendrite tip and exhibits a symmetric distribution which is similar to the dendrite pattern. Besides, the temperature in the solid region is always higher than that in the liquid, and the temperature-distance curves at different times are broadly similar, i.e., the temperature increases from a lower value to the maximum at the tip and then maintains a higher value until reaching another tip. As the distance further increases, i.e., approaching the far-field liquid, the temperature starts to decrease. It is noted that the maximum temperature does not keep increasing with dendrite evolution. When the released latent heat is not enough to counterbalance the effect of the imposed heat sink, the domain temperature decreases, e.g., from the 300 000th step to the 600 000th step.

Figure 7 shows the tip growth velocity and dimensionless temperature versus time for the 3D thermosolutal single dendrite growth. $\dot{q}_{\mathrm{LBM}} = 2.5 \times 10^{-5}$. As the dendrite grows, the temperature keeps decreasing, while the growth velocity increases.

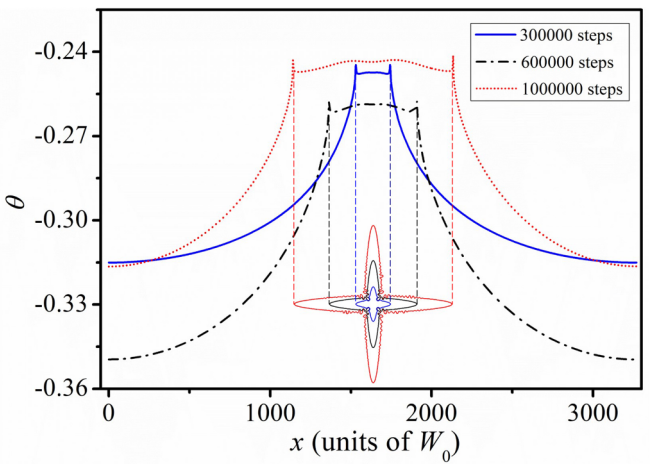


FIG. 6. Dimensionless temperature $\theta$ vs distance along the horizontal centerline of the 2D domain at the 300 000th, 600 000th, and 1 000 000th steps respectively. The inset is the dendrite contours at different time.

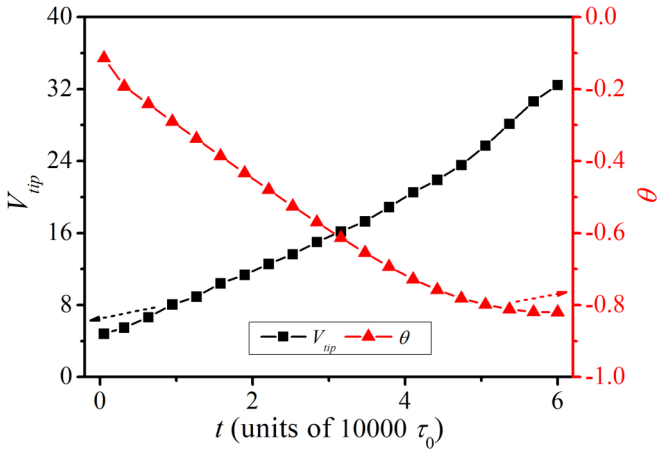


FIG. 7. Tip growth velocity $V_{\text{tip}}$ and dimensionless temperature $\theta$ vs time for the 3D thermosolutal single dendrite growth.

Figure 8 shows the effect of Le on dimensionless temperature at the 50 000th steps and the dendritic average growth velocity (from initialization to the 50 000th steps), in which $\dot{q}_{\text{LBM}} = 2.5 \times 10^{-5}$, and $\text{Le} = \infty$ means the temperature is independent of the position. As Le increases, the thermal propagation increases, i.e., the released latent heat diffuses rapidly, which tends to make the domain temperature uniform (see the decreasing maximum-minimum undercooling difference). The spreading heat decreases the thermal accumulation near the S-L interface, which increases the driving force for solidification and accelerates the dendrite growth. Furthermore, the relation between the average growth velocity $V_a$ and Le can be described by the following fitting function:

$$V_a = p_0 + \frac{p_1}{1 + p_2 \text{Le}^{p_3}}, \tag{23}$$

where $p_0 = 16.3$, $p_1 = -15.8$, $p_2 = 0.042$, and $p_3 = 0.76$ are constants dependent on the physical properties of the alloy. Two fitting indicators, namely reduced chi sq and adj. $r$ square [60], are used to characterize the fitting degree, which are 0.085 37 and 0.996 24 respectively, indicating a higher fitting degree.

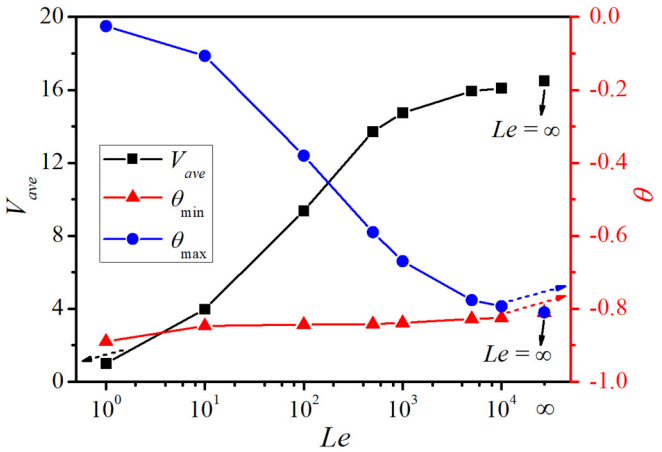


FIG. 8. Average growth velocity $V_{\text{ave}}$ and dimensionless temperature $\theta$ vs Le.

### B. Equiaxed multidendrite growth

#### *1. 2D equiaxed multidendrite growth*

Figure 9 shows the evolution of the 2D equiaxed multidendrite morphology including the phase field, temperature field, and solute field. The column corresponds to the snapshots at the 40 000th, 400 000th, 800 000th, and 1 200 000th steps from left to right. Twenty seeds are initialized (artificially) randomly in the domain, and each column corresponds to the distribution of the phase field, temperature field, and solute field at the same time. The domain size is 4096 × 4096 (i.e., 3276.8 × 3276.8 units of $W_0{}^2$ when $dx_{\text{min}} = 0.8$ units of $W_0$), and $\dot{q}_{\text{LBM}} = 4 \times 10^{-6}$. Different colors are used to distinguish the dendrites with different growth orientations. Initially, all dendrites grow independently, exhibiting a fourfold symmetry, and the secondary arms stretch out as the primary arms protrude into the undercooled melt.

As shown in the regions A and B in Fig. 9(f), the denser the distribution of dendrite, the more the released latent heat, and thus the higher the local temperature. The uneven distribution of the seeds causes a nonuniform temperature distribution, which in turn affects the development of the secondary arms. In particular, the secondary arms at region A are less developed than those at B due to lower undercooling (i.e., less driving force). When different dendrite arms meet and impinge, as marked by the circles in Fig. 9(d), the growth of the primary arms is blocked, and some side arms even overgrow the neighboring primary arms. Furthermore, the dendrite microsegregation and competitive growth are also reproduced under the coupled thermosolutal condition. As shown in Fig. 9(l), the interdendrite concentration is always higher due to solute accumulation.

Figure 10(a) shows the temperature fluctuations along the horizontal centerline of the computational domain corresponding to Figs. 9(e)–9(h). Because of the release of latent heat, the temperature is always higher at the growing S-L interface. The temperature-distance curves experience multiple local extreme points, indicating the complexity of thermal diffusion. Such complexity can also be revealed by the nonlinear variation of the dimensionless maximum and minimum temperature in the whole domain in Fig. 10(b). The domain temperature is controlled by the interaction between the imposed heat sink and released latent heat. As the dendrites grow, the released latent heat increases due to increasing S-L interface, which counteracts the effect of heat sink and makes the maximum temperature (i.e., the temperature at the interface) change slightly. But far from the interface, the sink effect dominates and decreases the temperature at late solidification.

#### *2. 3D equiaxed multidendrite growth*

Figure 11 shows the 3D simulation result of ten randomly distributed dendrites including the phase field, temperature field, and solute field at the 10 000th, 50 000th, and 150 000th steps, respectively. The domain size is 2048 × 2048 × 2048 units of $W_0{}^3$, which is equivalent to over eight billion meshes if a uniform mesh structure is employed. $\dot{q}_{\text{LBM}} = 5 \times 10^{-6}$ and $\theta = -0.2$. Similar to the 2D case in Fig. 9, colors are used to distinguish the dendrites with different growth orientations. All dendrites propagate outwards from the seed center independently and then impinge each other. The temperature

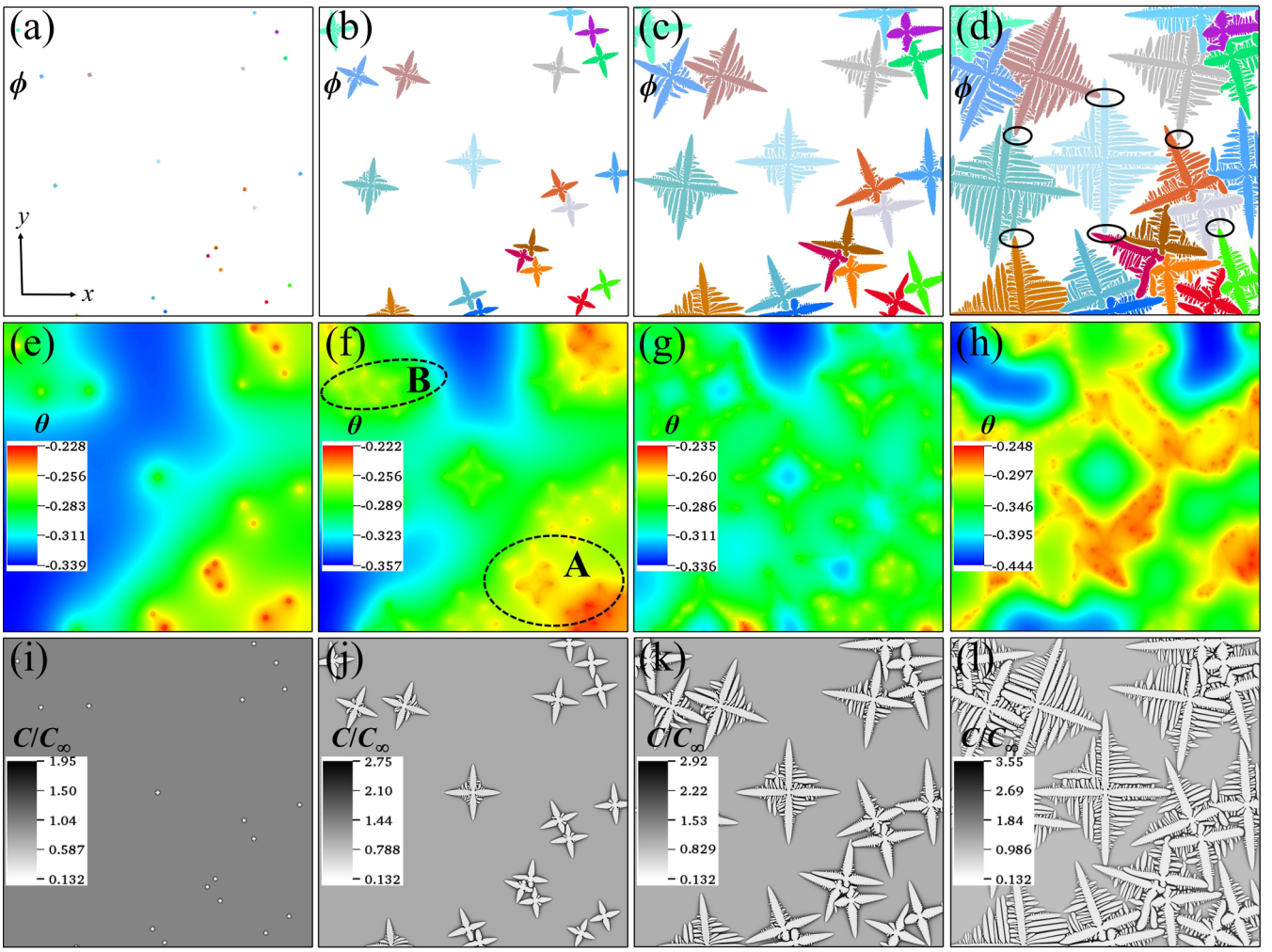


FIG. 9. Evolution of 2D equiaxed multiple dendrites including (a)–(d) phase field, (e)–(h) temperature field, and (i)–(l) solute field. The column corresponds to the snapshots at the 40 000th, 400 000th, 800 000th, and 1 200 000th steps from left to right. Twenty randomly distributed seeds are initialized in the domain.

reaches the local extreme at the S-L interface, and the thickness of the thermal boundary layer is significantly larger than that of the solutal boundary layer.

The combination of the parallel computing and adaptive hierarchical structure greatly improves the computing efficiency. The total elapsed time for the 2D equiaxed multidendrite case is about 17 h for a total 1 200 000 steps when 72 processes are employed, and for the 3D case it is about 415 h for a total 150 000 steps when 192 processes are employed. If uniform meshes are employed, in order to achieve such

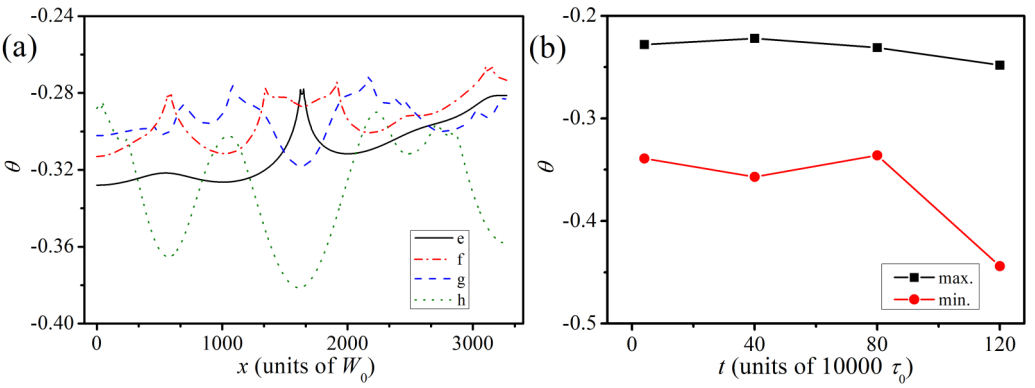


FIG. 10. (a) Temperature fluctuations along the horizontal centerline of the computational domain corresponding to the temperature field cloud maps shown in Figs. 9(e)–9(h). (b) The dimensionless maximum and minimum temperature at different time.

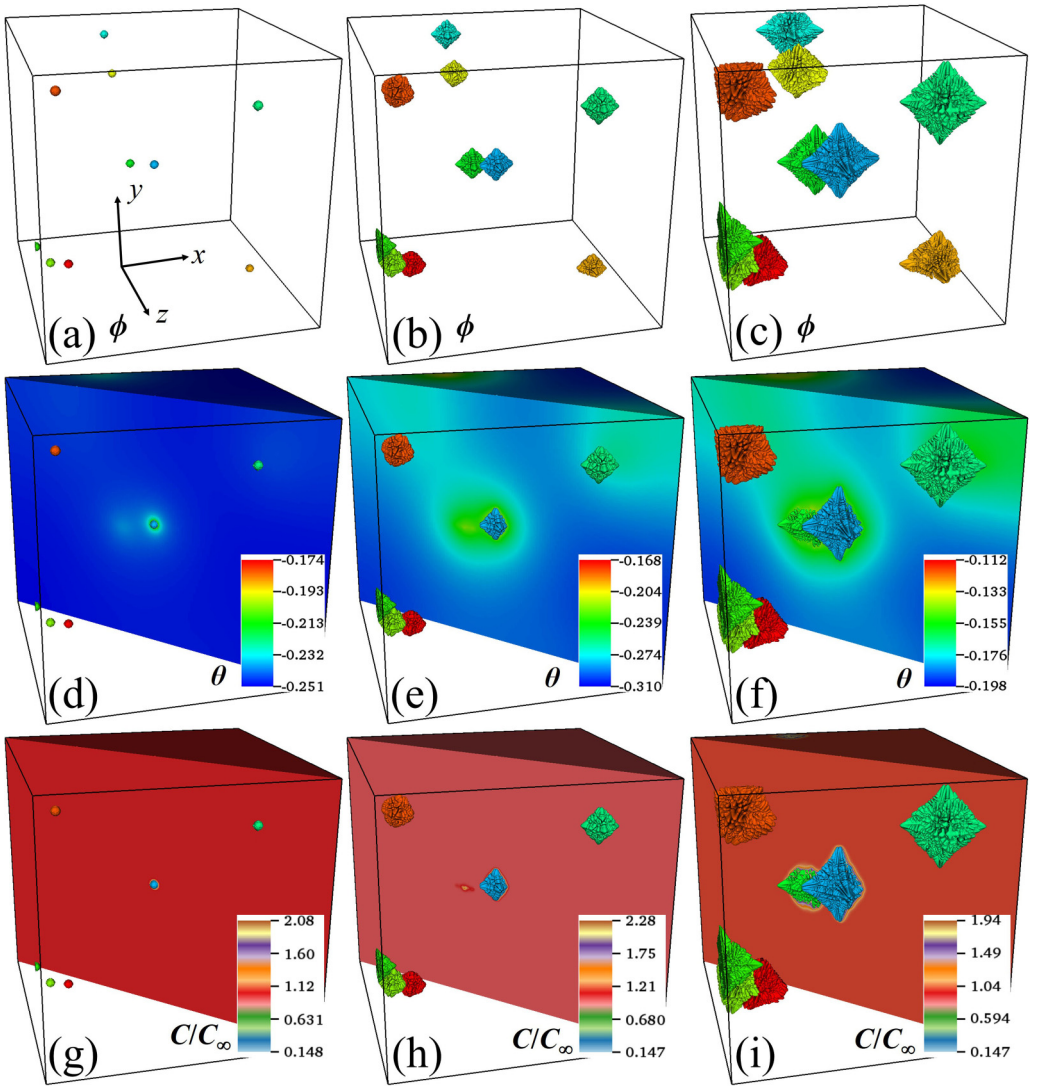


FIG. 11. Evolution of 3D equiaxed multiple dendrites including (a)–(c) phase field, (d)–(f) temperature field, and (g)–(i) solute field. The column corresponds to the snapshots at the 10 000th, 50 000th, and 150 000th steps from left to right. Ten randomly distributed seeds are initialized in the domain.

simulation scale, one will need lattice with billions of nodes [25], which makes it impractical to simulate microstructures over meaningful volumes of materials.

### C. Directional multidendrite growth

#### *1. 2D directional multidendrite growth*

Figure 12 shows the 2D directional multidendrite growth including the phase field, temperature field, and solute field at the 100 000th, 800 000th, 1 800 000th, and 2 800 000th steps, respectively. A periodic boundary condition is set at the two side walls while a zero-Neumann boundary condition is applied at both top and bottom sides for all variables including the phase field, solute concentration, and temperature. Each column corresponds to the distribution of the phase field, temperature field, and solute field at the same time. Twenty seeds are initialized (artificially) randomly at the domain bottom, and a uniform temperature gradient $G_\theta$ is set along the growth direction (i.e., $y^+$),

$$G_\theta = \frac{\theta_t - \theta_b}{Y}, \tag{24}$$

where $\theta_t = -0.18$ and $\theta_b = -0.2$ are the specified dimensionless temperature at the domain top and bottom, respectively, and $Y$ is the domain height. The domain size is $4096 \times 4096$ (i.e., $3276.8 \times 3276.8$ units of ${W_0}^2$ when $dx_{\min} = 0.8$ units of $W_0$), and $\dot{q}_{\mathrm{LBM}} = 1 \times 10^{-6}$. Different colors are used to distinguish the dendrites with different growth orientations.

The dendrites grow upwards with developed side branches and complex impingement. Some dendrites survive while others are blocked. Only nine dendrites can be observed at the final time step [see Fig. 12(d)]. The blocked dendrites, as circled in Fig. 12(d), are always those growing with larger deviation from the temperature gradient direction (i.e., $y^+$). Taking dendrites $D_1$ and $D_2$ for instance, the angles between the growing direction and the $y^+$ axis are 0° and 13.5°

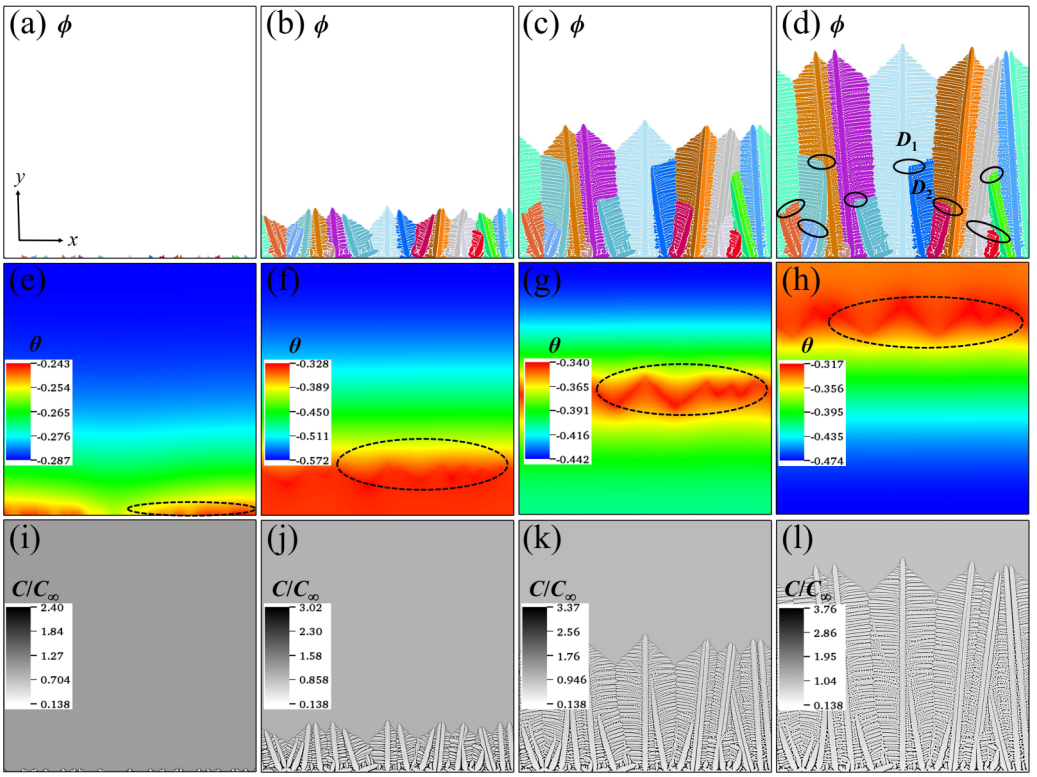


FIG. 12. Evolution of 2D directional multiple dendrites including (a)–(d) phase field, (e)–(h) temperature field, and (i)–(l) solute field. The column corresponds to the snapshots at the 100 000th, 800 000th, 1 800 000th, and 2 800 000th steps from left to right. Twenty randomly distributed seeds are initialized at the domain bottom.

respectively. The deviation from the $y^+$ makes dendrite $D_2$ finally blocked by dendrite $D_1$.

The maximum temperature evolves with the dendrite growth and always exhibits near the dendrite tip, as circled in Figs. 12(e)–12(h). Figure 13(a) shows the temperature distribution along the vertical centerline of the computational domain corresponding to Figs. 12(e)–12(h). The released latent heat during solidification makes the temperature-distance curves obtain extremes at the growing S-L interface. Figure 13(b) shows the dimensionless maximum and minimum temperature at different time in the whole domain. At early solidification, the heat sink dominates and the domain temperature keeps decreasing. As the dendrites evolve, the released latent heat starts to counteract the effect of heat sink, and the domain temperature rises. Controlled by both heat sink and latent heat, the domain temperature exhibits nonlinear change. In addition, similar to Fig. 9, the interdendrite concentration is significantly higher than that elsewhere.

### *2. 3D directional multidendrite growth*

Figure 14 shows the evolution of 3D directional multidendrite growth including the phase field, temperature field, and solute field. The column corresponds to the snapshots

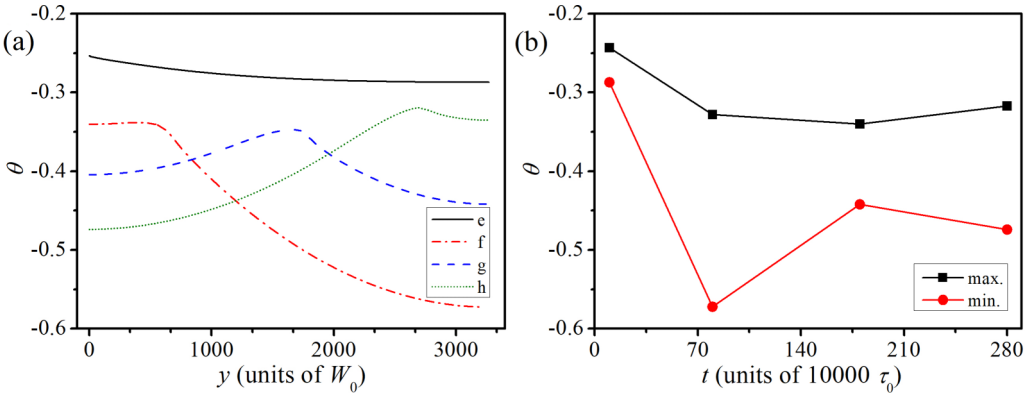


FIG. 13. (a) Temperature fluctuations along the vertical centerline of the computational domain corresponding to the temperature field cloud maps shown in Figs. 12(e)–12(h). (b) The dimensionless maximum and minimum temperature at different time.

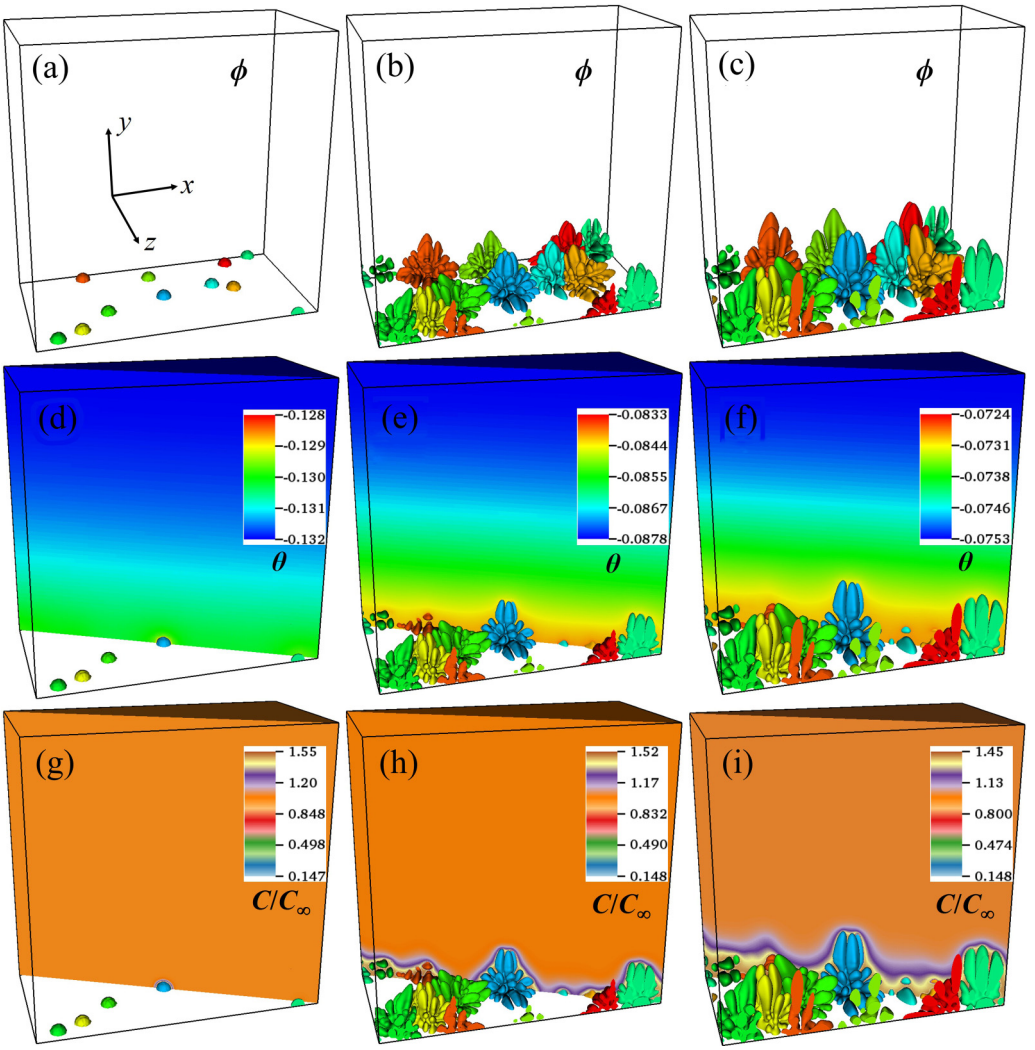


FIG. 14. Evolution of 3D directional multiple dendrites including (a)–(c) phase field, (d)–(f) temperature field, and (g)–(i) solute field. The column corresponds to the snapshots at the 10 000th, 150 000th, and 300 000th steps from left to right. Ten randomly distributed seeds are initialized at the domain bottom.

at the 10 000th, 150 000th, and 300 000th steps from left to right. The domain size is $1024 \times 1024 \times 512$ (i.e., $819.2 \times 819.2 \times 409.6$ units of ${W_0}^3$ when $dx_{\min} = 0.8$ units of $W_0$), $\dot{q}_{\mathrm{LBM}} = 5 \times 10^{-7}$, $\theta_t = -0.12$, and $\theta_b = -0.14$. Ten nuclei are randomly seeded at the domain bottom, and colors are used to distinguish the dendrites with different growth orientations. A periodic boundary condition is set at the four side walls, while a zero-Neumann boundary condition is applied at both top and bottom sides for all variables.

The nuclei grow towards the surrounding liquid under the control of the crystal anisotropy and then impinge with one another. The dendrite arms along the temperature gradient direction grows fastest. As expected from a large Le ($\sim 10^4$), the thermal boundary layer is wider than the solutal boundary layer. It is noted that a smaller heat sink is used in this case, which makes the effect of the latent heat become predominant. The accumulated heat near the dendrite tip reduces the driving force for solidification, which makes the dendrites grow slowly.

As the dendrites evolve, the computing time *per* time step increases due to increasing S-L interface area, i.e., more grids need to be generated to characterize the refined interface. In particular, the computing time for the current case increases from 1.1 h for the first 10 000 steps to 8 h for the last 10 000 steps when 120 processes are employed. Generally, the last 30% occupies 70–80% of the entire elapsed time, because the number of the grids, especially at the finest level, increases proportionally with the increasing S-L interface area [28].

## VI. CONCLUSIONS AND OUTLOOK

Typical cases are tested to illustrate the robustness and high efficiency of the proposed numerical scheme. Accordingly, the following three conclusions can be summarized:

(1) A general hierarchical structure is developed for the phase-field lattice-Boltzmann simulation with dissimilar time scales. The restriction on the time marching step is relaxed by constructing the multilevel data structure, and the number of the grid levels can be artificially selected in a reasonable range. Constructed on a massively parallel platform, the proposed numerical scheme can adjust the mesh distribution dynamically according to a gradient criterion. The developed

high performance computing scheme is successfully applied to simulate the coupled thermosolutal dendrite evolution.

(2) Numerical tests reveal that by employing the numerical scheme, the time step can be enhanced by two to three orders of magnitude in comparison with the explicit methods. Meanwhile, employing LBM avoids solving complicated coupled partial difference equations in an implicit time marching scheme. With the capability of parallel computing and adaptive hierarchical structure, the computing efficiency can be further improved by two to three orders of magnitude. Combining these two strategies can improve the overall computing efficiency at a very significant extent, which makes it viable to simulate large-scale (equivalently consisting of billions of meshes in a uniform-grid scheme) thermosolutal microstructure evolution with less computing overhead.

(3) The dendrite growth with realistic Lewis number $\sim 10^4$ is presented under fully coupled thermosolutal condition. Because of the release of latent heat during solidification, the temperature is always higher near the growing S-L interface. A simple analytical model is proposed to predict the relation between growth velocity and Lewis number. The growth morphologies of equiaxed and directional multidendrites are discussed. Influenced by the uneven temperature distribution, significant difference from the isothermal cases is observed in the development of dendrite arms.

The scales of the secondary dendrite arm spacing and the dendrite tip radius are typically in the range of 1–100 $\mu$m and 0.1–10 $\mu$m. To simulate a representative volume of a real casting (1–1000 $\mathrm{mm}^3$), a high performance computing scheme is a prerequisite to achieve high-efficiency large-scale phase-field simulations. However, strong assumptions, e.g., ignorance of liquid convection, use of binary alloys, and frozen temperature approximation, are still necessary to simulate multiple dendrites in 3D [61]. Considering that solidification is a multiscale, multiphysical, multicomponent problem in four dimensions (space and time), the current work in thermosolutal dissimilar time scales can help reveal the underlying solidification behaviors in a much more explicit way. The following aspects can be explored in a future work:

(1) Mechanism of fragmentation. Fragmentation occurs under nonequilibrium conditions and is largely dependent on the rapidly changing thermal conditions (e.g., recalescence and reheating).

(2) Columnar-to-equiaxed transition. Such transition usually occurs in the front of columnar dendrites where thermal effects play an important role in the crystal nucleation and grain remelting.

(3) Microstructure and phase selection. Both transition from primary to eutectic reaction and transient growth of dendrites emerging from the eutectic interface are closely related to local thermal conditions.

(4) Extension to additive manufacturing. The thermal condition changes abruptly during additive manufacturing, and consideration of the release of the latent heat during simulation can give more accurate prediction in the final microstructure-property relationship.

(5) Improvement of thermodynamical models. The thermal diffusion affects the calculation of multicomponent phase equilibrium by changing the local temperature, which improves the accuracy of multiscale multicomponent modeling in investigating solidification problems (e.g., grain sedimentation and solute segregation).

## ACKNOWLEDGMENTS

This work was financially supported by the National Natural Science Foundation of China (Grants No. U1537202 and No. U1764253), the Tsinghua-General Motors International Collaboration Project (Grant No. 20153000354), and the Tsinghua Qingfeng Scholarship (Grant No. THQF2018-15). The authors would also like to thank the National Laboratory for Information Science and Technology in Tsinghua University for access to supercomputing facilities.

## APPENDIX: DERIVATION OF EQ. (20)

The thermal diffusivity in the LBM is scaled by $d\tilde{x}_{\max}$ and $d\tilde{t}$, i.e.,

$$\alpha_{\mathrm{LBM}} = \frac{\tilde{\alpha}}{d\tilde{x}_{\max}^2/d\tilde{t}}, \tag{A1}$$

where $d\tilde{x}_{\max} = 2^{n_l-1} d\tilde{x}_{\min}$.

By combining Eqs. (19) and (A1), we obtain

$$\alpha_{\mathrm{LBM}} = \frac{r\mathrm{Le}}{2^{2n_l-1}N_d} \tag{A2}$$

where $\mathrm{Le} = \tilde{\alpha}/\tilde{D}$.

To match macroscopic thermal diffusivity, the relaxation time $\tau_{\mathrm{LBM}}$ in the LBM satisfies [30,42]

$$\tau_{\mathrm{LBM}} = \frac{3\alpha_{\mathrm{LBM}}\delta t}{\delta x^2} + \frac{1}{2}. \tag{A3}$$

By combining Eqs. (A2) and (A3), we can derive Eq. (20).

[1] R. Trivedi and W. Kurz, Int. Mater. Rev. **39**, 49 (1994).
[2] J. A. Dantzig and M. Rappaz, *Solidification* (EPFL, Lausanne, 2009).
[3] A. Zhang, J. Du, Z. Guo, Q. Wang, and S. Xiong, Metall. Mater. Trans. B **49**, 3603 (2018).
[4] J. C. Ramirez and C. Beckermann, Acta Mater. **53**, 1721 (2005).
[5] S. Wang, Z. P. Guo, X. P. Zhang, A. Zhang, and J. W. Kang, Ultrason. Sonochem. **51**, 160 (2019).
[6] J. Du, Z. Guo, A. Zhang, M. Yang, M. Li, and S. Xiong, Sci. Rep. UK **7**, 13600 (2017).
[7] A. Zhang, S. Liang, Z. Guo, and S. Xiong, Exp. Therm. Fluid. Sci. **88**, 472 (2017).
[8] I. Steinbach, Model. Simul. Mater. Sci. **17**, 073001 (2009).
[9] M. Asta, C. Beckermann, A. Karma, W. Kurz, R. Napolitano, M. Plapp, G. Purdy, M. Rappaz, and R. Trivedi, Acta Mater. **57**, 941 (2009).
[10] X. Fan, A. Zhang, Z. Guo, X. Wang, J. Yang, and J. Zou, J. Mater. Sci. **54**, 2680 (2019).
[11] W. J. Boettinger, J. A. Warren, C. Beckermann, and A. Karma, Annu. Rev. Mater. Res. **32**, 163 (2002).

[12] W. J. Boettinger and J. A. Warren, J. Cryst. Growth **200**, 583 (1999).

[13] A. J. Clarke, D. Tourret, Y. Song, S. D. Imhoff, P. J. Gibbs, J. W. Gibbs, K. Fezzaa, and A. Karma, Acta Mater. **129**, 203 (2017).

[14] T. Takaki, M. Ohno, T. Shimokawabe, and T. Aoki, Acta Mater. **81**, 272 (2014).

[15] D. Tourret, Y. Song, A. J. Clarke, and A. Karma, Acta Mater. **122**, 220 (2017).

[16] A. K. Boukellal, J. Debierre, G. Reinhart, and H. Nguyen-Thi, Materialia **1**, 62 (2018).

[17] A. A. Wheeler, W. J. Boettinger, and G. B. McFadden, Phys. Rev. A **45**, 7424 (1992).

[18] G. Boussinot, C. Hüter, R. Spatschek, and E. A. Brener, Acta Mater. **75**, 212 (2014).

[19] H. J. Diepers, C. Beckermann, and I. Steinbach, Acta Mater. **47**, 3663 (1999).

[20] A. Zhang, Z. Guo, and S. M. Xiong, Phys. Rev. E **97**, 053302 (2018).

[21] A. Zhang, S. Meng, Z. Guo, J. Du, Q. Wang, and S. Xiong, Metall. Mater. Trans. B **50**, 1514 (2019).

[22] I. Loginova, G. Amberg, and J. Ågren, Acta Mater. **49**, 573 (2001).

[23] L. Yuan and P. D. Lee, Model Simul. Mater. Sci. **18**, 055008 (2010).

[24] J. Rosam, P. K. Jimack, and A. M. Mullis, Acta Mater. **56**, 4559 (2008).

[25] J. Rosam, P. K. Jimack, and A. Mullis, J. Comput. Phys. **225**, 1271 (2007).

[26] Z. Guo, J. Mi, and P. S. Grant, J. Comput. Phys. **231**, 1781 (2012).

[27] J. Wu, Z. Guo, and C. Luo, Comput. Mater. Sci. **142**, 89 (2018).

[28] Z. Guo and S. M. Xiong, Comput. Phys. Commun. **190**, 89 (2015).

[29] J. Du, A. Zhang, Z. Guo, M. Yang, M. Li, F. Liu, and S. Xiong, Acta Mater. **161**, 35 (2018).

[30] T. Krüger, H. Kusumaatmaja, A. Kuzmin, O. Shardt, G. Silva, and E. M. Viggen, *The Lattice Boltzmann Method: Principles and Practice* (Springer, Cham, 2017).

[31] T. Takaki, R. Rojas, S. Sakane, M. Ohno, Y. Shibuta, T. Shimokawabe, and T. Aoki, J. Cryst. Growth **474**, 146 (2017).

[32] A. Zhang, J. Du, Z. Guo, Q. Wang, and S. Xiong, Philos. Mag. **99**, 2920 (2019).

[33] A. Cartalade, A. Younsi, and M. Plapp, Comput. Math. Appl. **71**, 1784 (2016).

[34] A. Younsi and A. Cartalade, J. Comput. Phys. **325**, 1 (2016).

[35] J. C. Ramirez, C. Beckermann, A. Karma, and H. J. Diepers, Phys. Rev. E **69**, 051607 (2004).

[36] R. Kobayashi, J. A. Warren, and W. C. Carter, Physica D **119**, 415 (1998).

[37] J. A. Warren, R. Kobayashi, A. E. Lobkovsky, and W. Craig Carter, Acta Mater. **51**, 6035 (2003).

[38] A. Karma, Phys. Rev. Lett. **87**, 115701 (2001).

[39] T. Haxhimali, A. Karma, F. Gonzales, and M. Rappaz, Nat. Mater. **5**, 660 (2006).

[40] D. Raabe, Model Simul. Mater. Sci. **12**, R13 (2004).

[41] P. L. Bhatnagar, E. P. Gross, and M. Krook, Phys. Rev. **94**, 511 (1954).

[42] A. A. Mohamad, *Lattice Boltzmann Method: Fundamentals and Engineering Applications with Computer Codes* (Springer, London, 2011).

[43] T. Seta, Phys. Rev. E **87**, 063304 (2013).

[44] J. Du, A. Zhang, Z. Guo, M. Yang, M. Li, and S. Xiong, Phys. Rev. Mater. **2**, 083402 (2018).

[45] J. Du, A. Zhang, Z. Guo, M. Yang, M. Li, and S. Xiong, ACS Omega **2**, 8803 (2017).

[46] A. Zhang, J. Du, Z. Guo, Q. Wang, and S. Xiong, Scr. Mater. **165**, 64 (2019).

[47] A. Zhang, Z. Guo, and S. M. Xiong, J. Appl. Phys. **121**, 125101 (2017).

[48] A. Zhang, J. Du, Z. Guo, and S. Xiong, Phys. Rev. E **98**, 043301 (2018).

[49] A. Zhang, J. Du, Z. Guo, Q. Wang, and S. Xiong, Metall. Mater. Trans. B **50**, 517 (2019).

[50] M. Berger and I. Rigoutsos, IEEE Trans. Syst., Man, Cybern. **21**, 1278 (1991).

[51] A. Dupuis and B. Chopard, Phys. Rev. E **67**, 066707 (2003).

[52] O. Filippova and D. Hänel, J. Comput. Phys. **147**, 219 (1998).

[53] X. Zhang, J. Kang, Z. Guo, S. Xiong, and Q. Han, Comput. Phys. Commun. **223**, 18 (2018).

[54] I. Rasin, W. Miller, and S. Succi, Phys. Rev. E **72**, 066705 (2005).

[55] W. Gropp, E. Lusk, and A. Skjellum, *Using MPI: Portable Parallel Programming with the Message-passing Interface* (MIT Press, Cambridge, MA, 2014).

[56] M. Bader, *Space-filling Curves: An Introduction with Applications in Scientific Computing* (Springer, Berlin, 2013).

[57] A. Zhang, J. Du, S. Meng, F. Liu, Z. Guo, Q. Wang, and S. Xiong, Comput. Mater. Sci. **171**, 109274 (2020).

[58] D. Wolf-Gladrow, J. Stat. Phys. **79**, 1023 (1995).

[59] J. Bragard, A. Karma, Y. H. Lee, and M. Plapp, Interface Sci. **10**, 121 (2002).

[60] R. A. Johnson and D. W. Wichern, *Applied Multivariate Statistical Analysis* (Pearson, Essex, 2014).

[61] W. Kurz, M. Rappaz, and R. Trivedi, Int. Mater. Rev. **72**, 1 (2020).